Spatial instabilities of light bullets in passively-mode-locked lasers

S. V. Gurevich*
Institute for Theoretical Physics, University of Münster, Wilhelm-Klemm-Strasse 9, D-48149 Münster, Germany and Center for Nonlinear Science, University of Münster, Corrensstrasse 2, D-48149 Münster, Germany

J. Javaloyes
Departament de Física, Universitat de les Illes Balears, C/ Valldemossa km 7.5, 07122 Mallorca, Spain
(Received 2 June 2017; published 9 August 2017)

Recently, the existence of robust three-dimensional light bullets (LBs) was predicted theoretically in the output of a laser coupled to a distant saturable absorber. In this paper, we analyze the stability and the range of existence of these dissipative localized structures and provide guidelines and realistic parameter sets for their experimental observation. In order to reduce the complexity of the analysis, we first approximate the three-dimensional problem by a reduced equation governing the dynamics of the transverse profile. This effective theory provides an intuitive picture of the LB formation mechanism. Moreover, it allows us to perform a detailed multiparameter bifurcation study and to identify the different mechanisms of instability. It is found that the LBs experience dominantly either homogeneous oscillation or symmetry-breaking transversal wave radiation. In addition, our analysis reveals several nonintuitive scaling behaviors as functions of the linewidth enhancement factors and the saturation parameters. Our results are confirmed by direct numerical simulations of the full system.

DOI: 10.1103/PhysRevA.96.023821

I. INTRODUCTION

Light bullets (LBs) consist of pulses of light that are simultaneously confined in the transverse and propagation directions. In the context of dissipative systems, LBs can be considered localized states (LSs) and are thus attractors of the dynamics. These hypothetical objects have attracted a lot of interest in the last 20 years for both fundamental and practical reasons. In practice, LBs should be addressable; that is, they should be individually turned on and off, and one can envision that they would circulate indefinitely within an optical cavity as elementary bits of information.

Traditionally, the optical confinement scenario that would lead to LBs is envisioned through conservative mechanisms in which a self-focusing nonlinearity compensates for the spreading effect of chromatic dispersion and/or diffraction. Seminal works demonstrated, however, that if the number of spatial dimensions is too large ($d_\perp \geqslant 2$), LBs are unstable and collapse [1], which is a result discovered earlier in the field of plasma physics [2]. Other confinement mechanisms were envisioned in forced dissipative system, and LBs were predicted in optical parametric oscillators [3] and bistable cavities [4–6] with instantaneous nonlinearities.

Recently, a regime of temporal localization was predicted and experimentally demonstrated in a semiconductor passively mode-locked laser [7]. Passive mode locking (PML) is a well-known method for achieving short optical pulses [8]. It is achieved by combining two elements, a laser amplifier providing gain and a nonlinear loss element, usually a saturable absorber. For proper parameters, this combination leads to the emission of temporal pulses much shorter than the cavity round-trip τ. It was shown in [7] that, if operated in the long-cavity regime, the PML pulses become individually addressable temporal LSs coexisting with the off solution. In this long-cavity regime, the round-trip time τ is made much longer than the semiconductor gain recovery time $\tau_g \sim 1$ ns, which is the slowest variable. Interestingly, this temporal localization regime was found to be compatible with an additional spatial confinement mechanism, which led to the theoretical prediction of a regime of stable three-dimensional LBs [9].

While preliminary results based upon direct numerical integration allowed finding some basic estimates of the stability range for a generic parameter set, a full bifurcation study of the system described in [9] is still lacking. However, a multiparameter analysis considering the various design factors of a passively mode-locked laser system would be of high relevance, particularly to experimental groups, as it would inform upon the proper parameter ranges in which an experimental realization may take place. In particular, assessing not only the range of existence of the LBs but also their destabilization mechanisms is of paramount importance. However, the LBs presented in [9] are particularly stiff multiple-time-scale objects in which the optical pulse is followed by a material "trail" that differs in extension by three orders of magnitude. This stiffness, which occurs in the temporal domain or, equivalently, along the propagation axis, is exacerbated by the presence of the transverse dimensions that make a bifurcation analysis of two- and three-dimensional LBs a challenging problem.

We perform the analysis in this paper in two steps. First, we approximate the solutions of the three-dimensional (3D) problem by the product of a slowly evolving transverse profile and a short pulse propagating inside the cavity. This allows us to obtain a reduced model governing the dynamics of the transverse profile. This effective theory allows us to consider the LBs as if they were static diffractive spatial autosolitons, similar to those in [10]. We show that the transverse profile is governed by an effective Rosanov equation which allows for a detailed multiparameter bifurcation study and also allows us to identify the different mechanisms of

*gurevics@uni-muenster.de

instability. For that purpose, we employ the continuation and bifurcation package PDE2PATH [11]. It is found that the light bullets experience dominantly either homogeneous oscillation or symmetry-breaking lateral wave radiation. In addition, our analysis reveals several nonintuitive scaling behaviors as a function of the linewidth enhancement factors and the saturation parameter. In the second stage, our predictions are confirmed by extensive direct numerical simulations of the spatiotemporal dynamics of the full system.

II. MODEL

We describe the passively mode-locked laser using the generic Haus partial differential equation (PDE) [8]. We consider a situation in which a broad-area gain chip is coupled to a distant saturable absorber (SA) with telescopic optics in self-imaging conditions, as in [12]. In this situation, each point of the gain section is mapped onto the absorber section and vice versa. The diffraction in our system is the result of the propagation within the active sections. We assume that it is considered sufficiently small to justify the use of the paraxial approximation, as in [13]. We also work in the limit of moderate gain G and saturable absorption Q such that the uniform field limit applies. In this context, the equation governing the evolution of the field profile $E(r_\perp,z,\sigma)$ over the slow time scale σ reads

$$\partial_\sigma E = \left\{\sqrt{\kappa}\left[1+\frac{1-i\alpha}{2}G(r_\perp,z,\sigma)-\frac{1-i\beta}{2}Q(r_\perp,z,\sigma)\right] -1+\frac{1}{2\gamma^2}\partial_z^2+(d+i)\Delta_\perp\right\}E(r_\perp,z,\sigma), \quad (1)$$

where γ is the bandwidth of the spectral filter representing, e.g., the resonance of a Vertical-Cavity Surface-Emitting Laser (VCSEL) [14], $\Delta_\perp=\partial_x^2+\partial_y^2$ is the transverse Laplacian, κ is the fraction of the power remaining in the cavity after each round-trip, and α and β are the linewidth enhancement factors of the gain and absorber sections, respectively. The amount of diffraction in the combined gain and absorber sections can be described by a diffraction length that was used in Eq. (1) to normalize the transverse space variables $r_\perp=(x,y)$. As such, the transverse domain size $L_\perp$ becomes a bifurcation parameter. For small $L_\perp$, the system is governed by its transverse boundary conditions, and conversely, localized states may occur when $L_\perp\gg 1$. The parameter d represents the small amount of field diffusion incurred, for instance, by the dependence of the reflectivity of the VCSEL distributed Bragg reflectors upon the angle of incidence. The longitudinal variable (z) is identified as a fast-time variable and represents the evolution of the field within the round-trip. The carrier dynamics reads

$$\partial_z G=\Gamma G_0-G(\Gamma+|E|^2)+\mathcal{D}_g\Delta_\perp G, \quad (2)$$

$$\partial_z Q=Q_0-Q(1+s|E|^2)+\mathcal{D}_q\Delta_\perp Q, \quad (3)$$

where G_0 is the pumping rate, $\Gamma=\tau_g^{-1}$ is the gain recovery rate, Q_0 is the value of the unsaturated losses, s is the ratio of the saturation energy of the gain and SA sections, and $\mathcal{D}_{g,q}$ are the scaled diffusion coefficients. In general, the noninstantaneous response of the active medium represented by the variable G implies a lack of parity along z for the LSs generated by Eqs. (1)–(3) (see [15] for details). In Eqs. (1)–(3) the fast time z has been normalized to the SA recovery time that we assume to be $\tau_{sa}=20$ ps. Setting $\gamma=40$ and $\Gamma=0.04$ corresponds to a FWHM of 250 GHz for the gain bandwidth and a carrier recovery time $\tau_g=500$ ps. Assuming a diffraction length of $l_\perp=1\,\mu$m and a domain size $L_\perp=190$ corresponds to a 190-μm broad-area device. The typical dimensions of the LB are $l_{LB}\sim 10\,\mu$m and $\tau_{LB}\sim 4$ ps. Finally, it was shown in [9] that carrier diffusion plays almost no role in the dynamics, so we set the diffusion coefficients $\mathcal{D}_{g,q}=0$. For proper system parameters, Eqs. (1)–(3) sustain the existence of stable three-dimensional light bullets as depicted in Fig. 1. The details regarding the numerical method used to solve Eqs. (1)–(3) can be found in Sec. A4 of Appendix. If not otherwise stated, all the data represented in the figures are dimensionless.

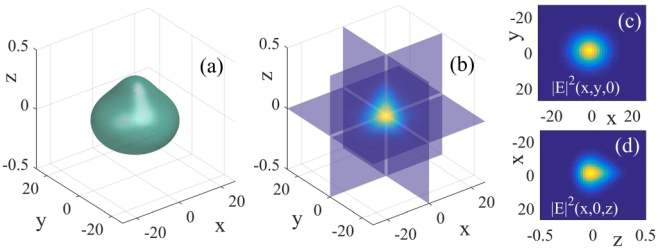

FIG. 1. Exemplary solutions of Eqs. (1)–(3) showing the intensity profile of a stable LB. (a) Isosurface at 1% of the maximal value. (b) Cross sections in the three orthogonal planes defined as $x=0$, $y=0$, and $z=0$. (c) and (d) The corresponding cross-section profiles. Parameters are $(\gamma,\kappa,\alpha,\beta,\Gamma,G_0,Q_0,s,d)=(40,0.8,1.5,0.5,0.04,0.425,0.354,30,10^{-2})$.

Exploiting the seminal work of New [16] and the fact that the LBs are composed of variables evolving over widely different time scales, one can find an approximate model governing the shaping of the transverse profile. We assume that the field reads $E(r_\perp,z,\sigma)=A(r_\perp,\sigma)p(z)$, with $p(z)$ being a short normalized temporal pulse of length τ_p that represents the temporal LS upon which the LB is built and $A(r_\perp,\sigma)$ being a slowly evolving amplitude. Separating the temporal evolution into the fast and slow parts corresponding to the pulse emission and the subsequent gain recovery allows us to find the equation governing the dynamics of A as

$$\partial_t A=(d+i)\left(\partial_u^2+\partial_v^2\right)A+f(|A|^2)A. \quad (4)$$

Defining $h(P)=(1-e^{-P})/P$, $P=|A|^2$, the function f reads

$$f(P)=(1-i\alpha)g(1+q)h(P)-(1-i\beta)qh(sP)-1; \quad (5)$$

see Sec. A1 for more details. We defined in Eqs. (4) and (5) the scaled spatial and temporal coordinates as $t=(1-\sqrt{\kappa})\sigma$ and $(u,v)=\sqrt{1-\sqrt{\kappa}}(x,y)$. The effective parameters are the gain normalized to threshold g and the normalized absorption q, $g=G_0/G_{th}$ and $q=Q_0/(\frac{2}{\sqrt{\kappa}}-2)$. We defined $G_{th}=\frac{2}{\sqrt{\kappa}}-2+Q_0$ as the threshold gain value above which the off solution $(E,G,Q)=(0,G_0,Q_0)$ becomes unstable. All the localized states are found below the threshold for which $G<G_{th}$ or, equivalently, $g<1$. We note that in the

representation given in Eqs. (4) and (5) in which the threshold is automatically unity, the only parameters that appear are (g,q,α,β,s) as the cavity losses κ have been factored out. Note, however, that Eqs. (1)–(3) are obtained in the limit of small gain and losses. A too strong departure from the good cavity limit would necessitate larger gain, which would induce additional nonlinearities. Here, the losses could not be factored out anymore.

Interestingly, Eq. (4), which governs the dynamics of the transverse profile, is a so-called Rosanov equation [10,17] that is known in the context of static transverse autosolitons in a bistable interferometer. In these works one assumes a monomode continuous-wave (cw) emission along the longitudinal propagation direction which allows, via the adiabatic elimination of the material variables, us to find an effective equation for the transverse profile. The nonlinear function $h(P)$ would correspond to a static saturated nonlinearity, i.e., $h(P) \to 1/(1+P)$. A similar result can be obtained by setting $\partial_z G = \partial_z Q = 0$ in Eqs. (1)–(3). However, the adiabatic approximation of the gain along the propagation direction would be incorrect for a semiconductor material, and the reaction time of the gain is known to profoundly affect the stability of spatiotemporal structures [6]. In order to validate our approach that consists of factoring the 3D light bullet into the product of temporal and spatial LSs, we will compare the results of the bifurcation analysis of the one-dimensional (two-dimensional) Rosanov model with the numerical predictions of the two-dimensional (three-dimensional) Haus equations.

We note that we operate in a parameter regime where the function $f(P)$ possesses two fixed points. One solution is unstable and corresponds to a lower-intensity temporal LS, while the stable fixed point corresponds to a higher-intensity LS. As such, the system is not bistable for the cw solution, preventing the existence of static transverse autosolitons. It is, however, bistable for the amplitude of the temporal LS whose spatial profile may, for proper parameters, coalesce into a transverse soliton. In the following, we will call the homogeneous spatial solution the temporal LS with a uniform spatial profile.

Spatial LSs can be found within the region of bistability of the homogeneous solution. As such, studying in which conditions the homogeneous solutions of Eqs. (4) and (5) develop a hysteresis region provides information about the proper parameters for spatial localization. This analysis is performed in Sec. A2 (see in particular Figs. 8 and 9). We summarize here our main results. The critical value of q_c above which one obtain a subcritical region as a function of the normalized gain g reads $q_c = 1/(s_c - 1)$. In the presence of a subcritical region, the folding point, i.e., the minimal value for the gain g_m for which one can obtain a nonzero solution [see, for instance, the lower red circle in Fig. 2(a)], can be approximated by

$$g_m = -\frac{W_{-1}(-e^{-1-\frac{q}{s}})}{1+q}, \tag{6}$$

with the Lambert W function W_n. The extent of the subcritical region in which one may expect spatial LSs is then $g \in [g_m, 1]$. The asymptotics in the limit of large saturation and large absorption simply read

$$\lim_{s\to\infty} g_m = \frac{1}{1+q}, \quad \lim_{q\to\infty} g_m = \frac{1}{s}. \tag{7}$$

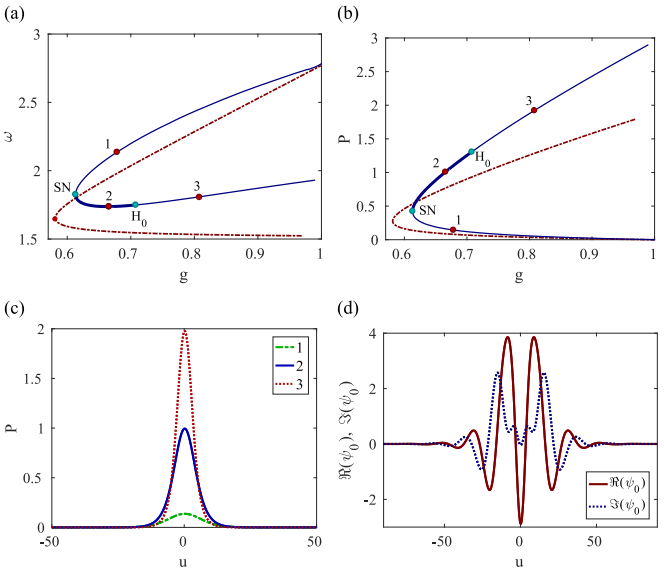

FIG. 2. Comparison between the behavior of the branch of the single LS solution (solid blue line) and that of the homogeneous solution (red dash-dotted line) calculated for $\alpha = 1.5$, $\beta = 0.5$. The evolution of (a) the spectral parameter ω and (b) the (peak) intensity P as a function of the normalized gain g is presented. (c) Three exemplary stationary LS profiles existing for different values of g. The LS is stable between the saddle-node bifurcation point (SN) and the Andronov-Hopf bifurcation point (H_0; thick blue line). (d) The real (solid red line) and imaginary (dashed blue line) parts of the corresponding critical eigenfunction ψ_0. Other parameters are $q = 1.27$, $s = 30$, $d = 0.01$.

Our results indicate that large values of the normalized absorption q and large saturation parameters s of course favor the breadth of a subcritical region, in agreement with intuition. However, less intuitive is that a saturation effect exists and marginal increases of the bistability domain are found for $s > 20$ and $q > 2$; see Fig. 9 in the Appendix for more details on the evolution of the folding point.

III. RESULTS

The single-LS solutions of Eqs. (4) and (5) can be found in the form

$$A(u,v,t) = a(u,v)\, e^{-i\omega t}, \tag{8}$$

where $a(u,v)$ is a complex amplitude with the localized field intensity $P = |a|^2$ and ω represents the carrier frequency of the solution. Substituting Eq. (8) into Eqs. (4) and (5), we are left searching for unknowns a and ω of the following equation:

$$(d+i)\left(\partial_u^2 + \partial_v^2\right)a + i\omega a + f(|a|^2)a = 0. \tag{9}$$

To directly track the LS solutions of Eq. (9) in parameter space, we make use of PDE2PATH [11,18], a numerical pseudo-arc-length bifurcation and continuation package for systems of elliptic partial differential equations. Details regarding the

numerical implementation of the problem can be found in Sec. A3.

Evolution of the folding point of the LS solution. As mentioned, the LS branch also possesses a folding point; see, for instance, the blue circle denoted SN in Fig. 2 which represents the minimal value of the gain at which localized states can be obtained. The analysis of the primary folding point of the LS branch g_{SN} as a function of the normalized absorption q and the saturation parameter s is detailed in Sec. A3. It is found that g_{SN} follows closely the evolution of the folding point of the uniform solution g_m with q and s (compare Figs. 9 and 10 of the Appendix, respectively). That is, our predictions for the evolution of the folding point of the homogeneous solution hold also for the LS branch, and our approximate analytical expression can be used as a guideline. The one-dimensional folding point is always shifted a few percent toward higher current values compared to the uniform case [see Figs. 2(a) and 2(b) and compare the red and blue curves]. A similar shift for the two-dimensional case exists with respect to the one-dimensional situation (see Fig. 10 in the Appendix).

Bifurcation analysis in one dimension. We now turn our attention to the possible mechanisms of instability occurring for increased values of the gain, and we present in Fig. 2 the bifurcation diagram of Eq. (9) as a function of g calculated for $\alpha = 1.5$ and $\beta = 0.5$. In particular, Fig. 2(a) represents the spectral parameter ω of the homogeneous solution (red dash-dotted line) and that of the one-dimensional LS (solid blue line) as a function of the gain g, while the power P as a function of g for both homogeneous (dash-dotted red line) and LS (solid blue line) solutions is depicted in Fig. 2(b). In the case of the LS we plot the peak intensity of the solution. We note that the bistability range of the single LS solution is contained in that of the homogeneous one. In addition, in Fig. 2(c) we depict three exemplary stationary LS profiles that exist for different values of g, as indicated by enumerated labels in Figs. 2(a) and 2(b). The power of the LS changes significantly along the branch, leading to the formation of narrow peaks of high intensity at the upper power branch.

Apart from the overall information regarding the branch morphology, the linear stability of a particular LS solution along the branch can be obtained directly during continuation. The stability analysis of Eqs. (4) and (5) reveals the existence of several neutral eigenvalues, corresponding to the translation, phase, and Galilean invariances (cf. Refs. [19,20] for static autosolitons). The results of the linear stability analysis are shown in Figs. 2(a) and 2(b). Here, thick (thin) blue curves correspond to stable (unstable) LS solutions. The LS stability domain lies between the saddle-node bifurcation point (SN) and the Andronov-Hopf (AH) bifurcation point (H_0). There, the branch of the LS gets destabilized via symmetric oscillations, i.e., a breathing of the LS profile (see Video 1 in the Supplemental Material [21]). An example of the real (solid red line) and imaginary (dashed blue line) parts of the critical eigenfunction ψ_0 associated with this breathing instability is shown in Fig. 2(d).

We note that it was shown in [9] that, similar to the case of static autosolitons [17,19], the branch of the one-dimensional LS forms a spiral in the (g,ω) plane for vanishing linewidth enhancement factors of both the gain and absorber sections.

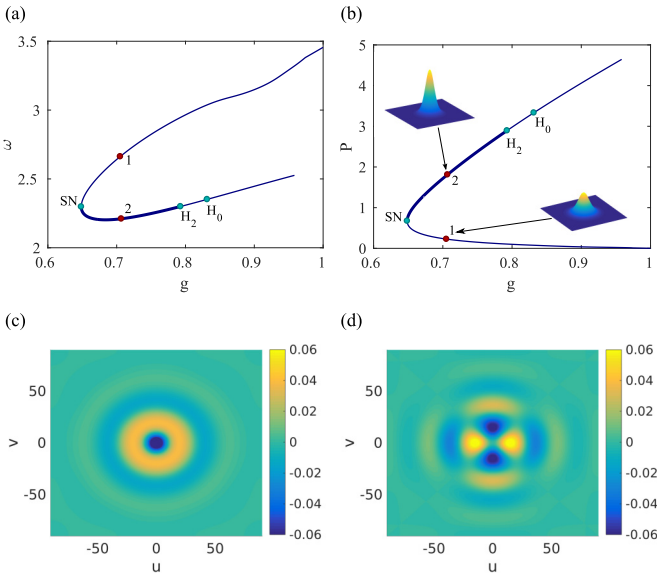

FIG. 3. Bifurcation diagram for a two-dimensional LS obtained for $\alpha = 1.7, \beta = 0.5$ as a function of the gain g, showing the evolution of (a) the spectral parameter ω and (b) the peak intensity P. The LS is stable between the saddle-node bifurcation point (SN) and the AH bifurcation point (H_2; thick blue line). The secondary AH bifurcation point is indicated as H_0. Two insets in (b) show intensity profiles, corresponding to unstable (labeled 1) and stable (labeled 2) LS solutions obtained at the same gain value $g = 0.705$. (c) and (d) The real parts of both $n = 0$ and $n = 2$ critical modes calculated at $g = 0.68$, respectively. Other parameters are the same as in Fig. 2.

We show here that, for more realistic values of (α,β), one finds a simpler branch structure that possesses a single fold. Our analysis of the evolution of the spiral structure of the branch and of the spectral parameter ω as a function of the gain g for small values of (α,β) can be found in Fig. 11 in the Appendix. We also note that for these more realistic values of (α,β) the breadth of the stable region is more extended, $\Delta g = g_{H_0} - g_{SN} \sim 0.1$, while $\Delta g \sim 0.03$ in [9]. These results indicate that the range of stable LB existence can be widely improved by the proper design of the experimental devices.

Bifurcation analysis in two dimensions. We performed a similar analysis in two transverse dimensions obtained for fixed values of $\alpha = 1.7$ and $\beta = 0.5$. Our results are presented in Fig. 3, where the dependence of the evolution of the spectral parameter ω [Fig. 3(a)] and the peak intensity P [Fig. 3(b)] on the gain g is shown. Note that the overall morphology of the two-dimensional LS branch resembles the one-dimensional behavior (compare Fig. 2). However, it turns out that a richer dynamics occurs and that additional modes of instability are found in two transverse dimensions. Besides a symmetrical radiation mode [see Fig. 3(c)] leading to an Andronov-Hopf bifurcation, similar to that in the one-dimensional case and also denoted H_0, compression-elongation oscillations in the two orthogonal directions are also possible [see Fig. 3(d)], which correspond to a bifurcation point denoted H_2. By defining the polar angle ϕ in the transverse plane, we can summarize the situation by saying that the point spectrum of the two-dimensional LS contains modes $\propto e^{in\phi}$ with $n = 0, \pm 2$. The mode with $n = 0$ results in a symmetrical change in the size of

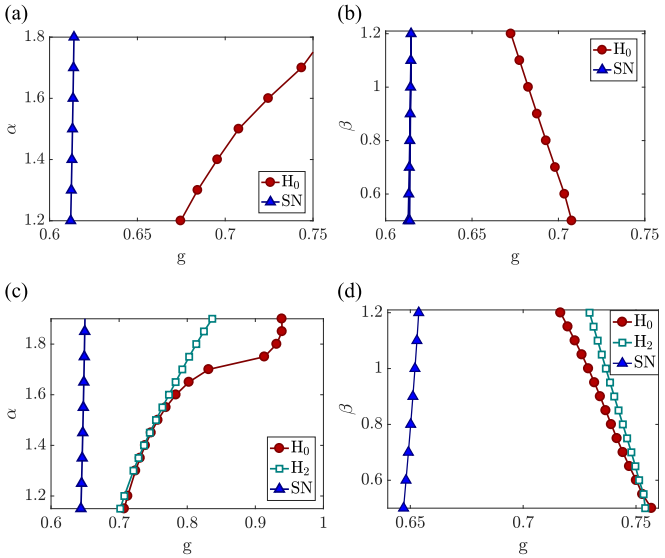

FIG. 4. (a) and (b) One-dimensional stability diagrams showing the threshold for the fold (blue triangles) and $n = 0$ AH bifurcations (red circles) in terms of the dependence of α on the gain g for (a) $\beta = 0.5$ and (b) $\alpha = 1.5$. (c) and (d). The same stability diagrams in two dimensions. Green squares depict the Andronov-Hopf line corresponding to the $n = 2$ instability. The range of stability grows with α and shrinks with β.

the LS, and $n = \pm 2$ correspond to a deformation of the LS in two perpendicular directions. Figures 3(c) and 3(d) show the real parts of $n = 0$ and $n = 2$ critical modes, respectively.

Our linear stability analysis indicates that similar to the one-dimensional case, the LS solution appears in a saddle-node bifurcation (SN) at low gain, while at high current the dominant mechanism of instability consists of an AH bifurcation at point H_2, where the corresponding $n = \pm 2$ modes become unstable (see Video 2 in the Supplemental Material [21]). That is, the thick (thin) blue curve in Figs. 3(a) and 3(b) corresponds to the stable (unstable) LS. In addition, two insets in Fig. 3(b) show intensity distributions, corresponding to unstable (labeled 1) and stable (labeled 2) parts of the LS branch obtained at the same gain value $g = 0.705$. Finally, the AH bifurcation point H_0 indicates a secondary instability of the LS with respect to modes with $n = 0$ (see Video 3 in the Supplemental Material [21]). Here, additional symmetrical oscillations of the LS shape are expected. Notice that the order of both AH bifurcations strongly depends on the linewidth enhancement factors of both gain and absorber sections.

Range of existence of the single LS. In [9], the linewidth enhancement factors of both the gain and absorber sections were set $\alpha = \beta = 0$ as a demonstration that the carrier-induced self-focusing effects played no role in the LB formation and that the confinement mechanism was different than the one found in conservative systems as in [1]. In this section, we study the influence of α and β factors that are set to more typical values, and we find that an extended range of stability exists by mapping the position of points H_0 and H_2 limiting the existence of stable LBs at high current. Adding to these results the evolution of the folding point SN allows us to disclose the range of existence of stable LSs in one and two transverse spatial dimensions.

As we mentioned above, in the one-dimensional case, at high current the dominant mechanism of instability consists of an Andronov-Hopf bifurcation H_n, with $n = 0$, whereas in the two-dimensional case we identified several modes of destabilization, one where the amplitude of the LS oscillates uniformly in space ($n = 0$) and another where the breadth of the LS breathes ($n = 2$). In order to study the influence of the α and β factors on the stability range of the single-LS solution we perform a two-parameter continuation of the fold and AH bifurcation points as a function of the gain g and the linewidth enhancement factors of the gain and the absorber sections. Our results are depicted in Fig. 4.

Figures 4(a) and 4(c) represent the stability diagrams in the (g,α) plane for the fixed value of $\beta = 0.5$ for one and two spatial dimensions, respectively. Here, blue triangles indicate the fold threshold, whereas red circles stand for the boundary of the AH bifurcation with $n = 0$. In addition, in Fig. 4(c) green squares depict the second AH line, $n = 2$. Note that depending on the relation between α and β, one of these two oscillation modes can govern the primary instability threshold. Our results reveal that in both one and two dimensions the range of the stability increases toward higher α values. Although the fold position remains almost constant for increasing α, both AH lines move toward higher currents. However, the width of the stability region strongly depends on β, as shown in Figs. 4(b) and 4(d), where the stability diagram for increasing β and a fixed moderate value of $\alpha = 1.5$ is presented for both one- and two-dimensional continuations. Here, in both cases the range of stability decreases for growing β.

Finally, we performed a similar analysis as a function of the saturation parameter s as shown in Fig. 5. One notices that

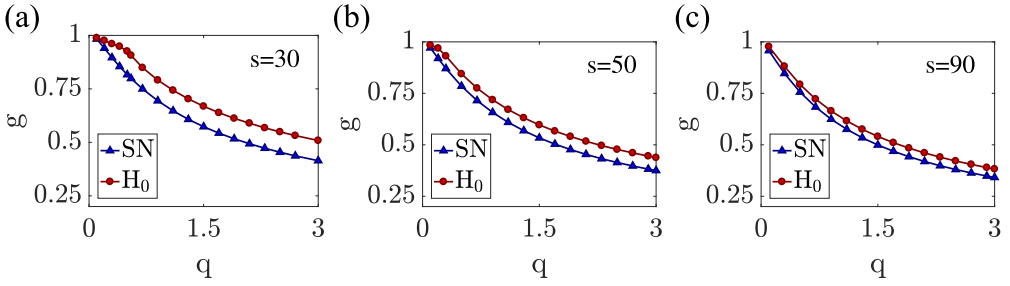

FIG. 5. One-dimensional stability diagrams showing the threshold for the fold (blue triangles) and the $n = 0$ AH bifurcations (red circles) in terms of the dependence of s on the gain g for $(\alpha,\beta) = (1.5,0.5)$. The range of stability shrinks for too large values of s. Similar trends are found in in two dimensions.

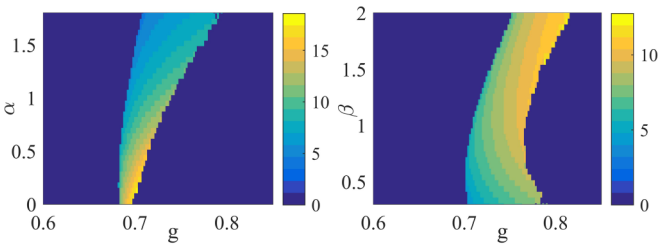

FIG. 6. Two-dimensional bifurcation diagram showing the region of stable existence of the LBs by integrating the two-dimensional Haus equation in (x,z) as a function of the gain g and the parameters α (left) and β (right). The color code represents the energy of the LB $\mathcal{E}$. The range of stability increases with α and decreases for small values of β, in agreement with Fig. 4. Similar trends were found in three dimensions. Parameters are $(\gamma,\kappa,\Gamma,Q_0,s,d) = (40,0.8,0.04,0.3,30,10^{-2})$ and $\beta = 0.5$ (left), $\alpha = 1.5$ (right).

for generic values of $(\alpha,\beta) = (1.5,0.5)$, the stability region *decreases* if the saturation parameter s gets too large, which is a counterintuitive result.

Numerical simulations of the Haus model. By using the guidelines obtained from the analysis of the homogeneous and transverse solutions, we now turn our attention to the predictions obtained by directly integrating Eqs. (1)–(3); the details of the numerical methods are given in Sec. A4. Our results are summarized in Fig. 6, in which we plot the energy of the LB, $\mathcal{E} = \iint |E|^2 dxdz$, and depict the region of stable existence as a function of the gain g and the linewidth enhancement factors α and β. Nicely, the dominant trends predicted by analyzing the effective equation of the transverse profile equation (4) are confirmed, a strong increase of the stable region with α and a moderate decrease for increasing β. In Video 4 in the Supplemental Material [21], we depict the instability mechanisms in two dimensions that correspond to H_0, as predicted, while in three dimensions, the dominant mechanism is governed by the H_2 instability (see Video 5 in the Supplemental Material [21]).

The transverse and longitudinal FWHM, the frequency shift ω, and drifting speed υ of the LBs are presented in Sec. A4.

A behavior similar to that predicted in Fig. 5 can be found when performing the integration of the Haus model in Eqs. (1)–(3) as a function of the saturation parameter s. Our results are summarized in Fig. 7, where we represent the energy; the other parameters of the solutions are depicted in Sec. A4. The dominant trends of a decrease in the region of existence with increased values of s is confirmed.

IV. CONCLUSION

In conclusion, we discussed how the dynamics of 3D light bullets can be successfully approximated in a wide parameter range by a simplified model governing the dynamics of the transverse profile. The bifurcation analysis of this effective model allows us to obtain guidelines regarding the existence and stability of the LBs found in the full problem. We have found that, as a function of the gain, the stability range is governed by the evolution of a lower limit point where the LB solution ceases to exist and an upper one where the system develops a breathing instability that can result either in a homogeneous oscillation of the profile or in orthogonal compression-elongation oscillations. We have found that, contrary to intuition, too large saturation parameters or modulation of the losses are either detrimental or irrelevant to the range of stability of the LBs. Finally, direct numerical simulations performed on a High Performance Computer of the full system confirmed the predictions of the simplified model. In our analysis we have found that the mechanism of instability of the LBs is essentially that of the transverse profile. Yet we believe that additional instabilities may take place for larger values of (α,β) for which the temporal LS that acts as the backbone of the spatial soliton can become unstable. Finally, instabilities that do not pertain to either the spatial or the temporal degree of freedom but to both simultaneously cannot be ruled out and will be a topic of further studies.

ACKNOWLEDGMENTS

S.G. acknowledges the Universitat de les Illes Balears for funding a stay where part of this work was developed. J.J. acknowledges J. Arbona for technical support regarding the UIB cluster Foner, the project COMBINA (TEC2015-65212-C3-3-P AEI/FEDER UE), and the Ramón y Cajal fellowship. J.J. and S.G. thank C. Schelte for a careful reading of the manuscript.

APPENDIX

1. Derivation of the effective Rosanov equation

We assume that the field reads $E(r_\perp,z,\sigma) = A(r_\perp,\sigma)p(z)$, with a short normalized temporal pulse $p(z)$ of length τ_p and a slowly evolving amplitude $A(r_\perp,\sigma)$. Next, we use the fact that, during the emission of a LB, the stimulated terms are

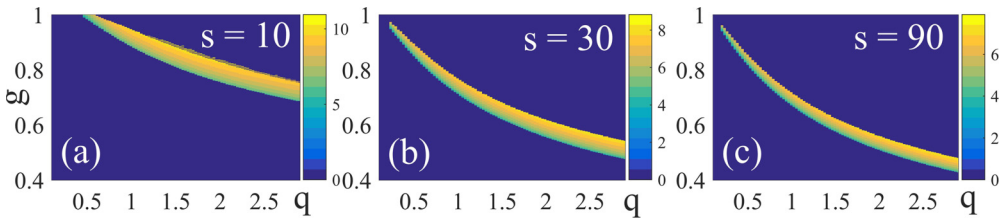

FIG. 7. Two-dimensional bifurcation diagram showing the region of stable existence of the LBs by integrating the two-dimensional Haus equation as a function of the gain g and the modulation of the absorption q. The color code represents the energy of the LB $\mathcal{E}$ for increasing values of the saturation parameter s. We find that the range of stability decreases with increasing values of s. Similar trends were found in three dimensions. Parameters are $(\gamma,\kappa,\alpha,\beta,\Gamma,d) = (40,0.8,1.5,0.5,0.04,10^{-2})$.

dominant in Eqs. (2) and (3), i.e., $|E|^2 \gg 1$, such that

$$-\int_0^{\tau_p} G|E|^2 dz \simeq \int_0^{\tau_p} \partial_z G\, dz = G_f - G_i, \quad \text{(A1)}$$

with G_i (G_f) being the gain before (after) the pulse emission (see [16,22] for more details). By integrating Eq. (2) in the regime $|E|^2 \gg 1$ we find that $G(z) = G(0)\exp(-\int_0^z |p|^2|A|^2 dz')$ and $G_f = G_i \exp(-|A|^2)$. Considering Eq. (3) with similar arguments, one finds $Q_f = Q_i \exp(-s|A|^2)$. Multiplying the field equation (1) by $\bar{p}$, integrating over the pulse length, neglecting the contribution $\gamma^{-1}\dot{p}$, and using the above expression of the stimulated terms, we find that the equation governing the dynamics of the transverse profile reads

$$\partial_\sigma A = (d+i)\Delta_\perp A + A\,F(|A|^2). \quad \text{(A2)}$$

The expression of the nonlinear function F is

$$F = \sqrt{\kappa}\left[1 + \frac{1-i\alpha}{2} G_0 h(P) - \frac{1-i\beta}{2} Q_0 h(sP)\right] - 1,$$

with $h(P) = (1-e^{-P})/P$. We replaced in the expression of F the values of the gain and the absorption at the beginning of the pulse with their equilibrium values by taking advantage of the long-cavity limit. It allows us to assume that the gain and absorption entirely lose their memory at the next round-trip.

The lasing threshold above which the off solution $(E, G, Q) = (0, G_0, Q_0)$ becomes unstable is

$$G_{th} = \frac{2}{\sqrt{\kappa}} - 2 + Q_0. \quad \text{(A3)}$$

As we operate in the region below threshold in which the temporal LSs are bistable with the trivial off solution, we define the gain normalized to threshold and the normalized absorption q as

$$g = G_0/G_{th}, \quad q = Q_0/\left(\frac{2}{\sqrt{\kappa}} - 2\right). \quad \text{(A4)}$$

Defining the scaled spatial and temporal coordinates as $t = (1-\sqrt{\kappa})\sigma$ and $(u,v) = \sqrt{1-\sqrt{\kappa}}\,(x,y)$ yields the normalized equations

$$\begin{aligned}\partial_t A &= (d+i)\left(\partial_u^2 + \partial_v^2\right)A + f(|A|^2)A, f(P)\\ &= (1-i\alpha)g(1+q)h(P) - (1-i\beta)qh(sP) - 1,\end{aligned}$$

where we define $F = f/(1-\sqrt{\kappa})$ and $P = |A|^2$.

2. Behavior of the homogeneous solution

The monochromatic solutions of Eqs. (4) and (5), denoted as $A = \sqrt{P}\exp(-i\omega t)$ with $P \in \mathbb{R}$, are given by $\mathrm{Re}(F) = 0$, which yields the implicit relation between gain and power

$$g = \frac{1+qh(sP)}{(1+q)h(P)}. \quad \text{(A5)}$$

As we consider the transverse profile of a LB, P actually corresponds to the power carried by the temporal LS, and the multiple solutions of Eq. (A5) should be identified with temporal LSs with different power densities. Once P is known, the carrier frequency of the solution can be found independently solving

$$\omega = \alpha g(1+q)h(P) - \beta q h(sP). \quad \text{(A6)}$$

Supercritical-subcritical transition point. A simple Taylor expansion of Eq. (A5) around the threshold gives the relation

$$g = 1 + p\frac{1+q(1-s)}{2(1+q)}. \quad \text{(A7)}$$

As such, the solution curve experiences a transition from supercritical toward subcritical when

$$1 + q_c(1-s_c) = 0, \quad \text{(A8)}$$

yielding a relation between the critical saturation s_c and the breadth of the absorber modulation q_c.

High-power branch. The upper solution branch, for which the values of P are large, can be approximated by replacing the nonlinear function $h(P)$ by its asymptotic value $h \sim 1/P$, such that Eq. (A5) takes the form

$$g(P) \simeq \frac{P + \frac{q}{s}}{1+q} \sim \frac{P}{1+q}, \quad \text{(A9)}$$

where we used the large-saturation approximation. The evolution of the solution from the supercritical toward the subcritical regime is depicted in Fig. 8(a), along with the asymptotic regimes for low and high intensities.

Folding-point approximation. The folding point is achieved at powers at which the saturable absorber is saturated but the gain is not. We replace only $h(sP)$ by its high-power expansion in Eq. (A5) to find

$$g(P) = \frac{P + \frac{q}{s}}{(1+q)(1-e^{-P})}. \quad \text{(A10)}$$

Searching for the folding point as a minimum of $g(P)$ yields a solution P_m that is only a function of q/s and reads

$$P_m\left(\frac{q}{s}\right) = -1 - \frac{q}{s} - W_{-1}(-e^{-1-\frac{q}{s}}), \quad \text{(A11)}$$

with $W_n(z)$ being the Lambert W function. We define the value of the gain at the folding point as $g_m = g(P_m)$ as it is a measure of the extent of the subcritical region

$$g_m = -\frac{W_{-1}(-e^{-1-\frac{q}{s}})}{1+q}. \quad \text{(A12)}$$

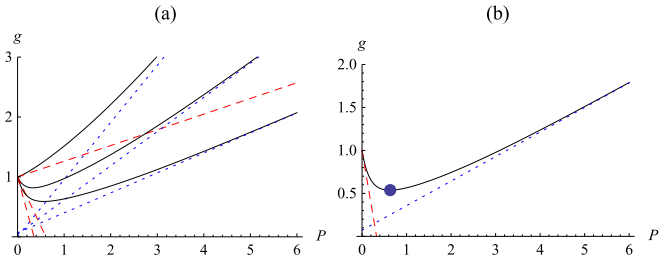

FIG. 8. (a) Evolution of the bistability regime for $s = 10$ and increasing values of $q = 0.05, 0.75$, and 2 (black lines). (b) Approximation of the folding point (P_m, g_m) for $s = 10$ and $q = 2.5$ (blue circle). In both cases the homogeneous solution is represented by a black line, and the asymptotic expansions for low and high power are represented by dashed red and dotted blue lines, respectively.

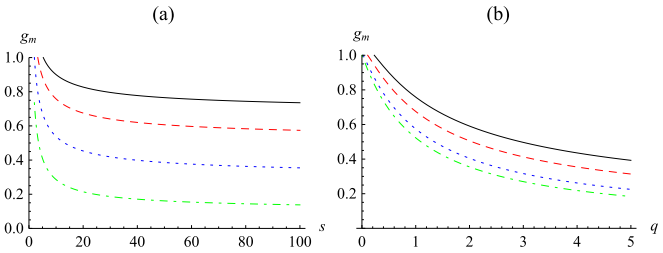

FIG. 9. (a) Evolution of the approximation of the folding point as a function of s and different values of q that correspond to $q = 0.5$ (solid black line), $q = 1$ (dashed red line), $q = 2.5$ (dotted blue line), and $q = 10$ (dash-dotted green line). (b) Evolution of the approximation of the folding point as a function of s and different values of q that correspond to $q = 0.5$ (solid black line), $q = 1$ (dashed red line), $q = 2.5$ (dotted blue line), and $q = 10$ (dash-dotted green line).

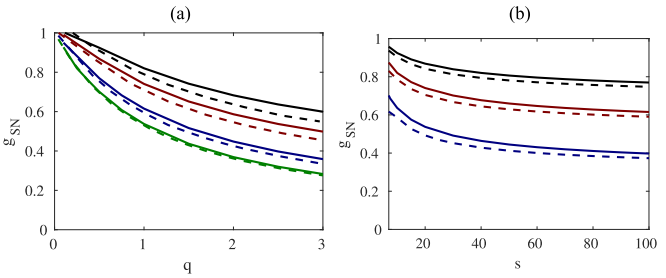

FIG. 10. (a) Continuation of the folding point g_{SN} of a single LS branch as a function of the normalized absorption q and different values of s that correspond to $s = 10$ (black lines), $s = 20$ (red lines), $s = 100$ (blue lines), and $s = 1000$ (green lines). (b) Continuation of g_{SN} of a single LS branch as a function of s and different values of q that correspond to $q = 0.5$ (black lines), $q = 1$ (red lines), and $q = 2.5$ (blue lines). Dashed (solid) lines in both panels indicate one- (two-) dimensional continuation.

The accuracy of our approximation is depicted in Fig. 8(b) by a blue circle. One can see that it is indistinguishable from the exact value.

Finally, while the solution of Eq. (A12) using the Lambert function is perhaps complicated, the asymptotic values of g_m in the limit of large saturation and large absorption are simply

$$\lim_{s\to\infty} g_m = \frac{1}{1+q}, \quad \lim_{q\to\infty} g_m = \frac{1}{s}. \tag{A13}$$

The scaling behavior of the folding point as a function of s using Eq. (A12) is represented in Fig. 9(a). We note that the asymptotic behavior in Fig. 9(a) can be obtained only for very large values of s. Similarly, the curves in Fig. 9(b) converge toward $g_m = s^{-1}$ for unrealistically large values of q. However, the behavior predicted by Eq. (A13) is qualitatively verified.

3. Bifurcation analysis of the Rosanov equation

a. Numerical method

The LS solutions of Eqs. (4) and (5) can be found in the form $A(r,t) = a(r)\,e^{-i\omega t}$, where $r = (u,v)$ are normalized transverse spatial coordinates, $a(r)$ is the complex amplitude with the field intensity $P = |a|^2$ localized around some point in space, and ω is the spectral parameter. To directly track LS solutions of Eq. (9) in the parameter space, we make use of PDE2PATH [11,18], a numerical pseudo-arc-length bifurcation and continuation package for systems of elliptic partial differential equations over bounded multidimensional domains which is based on the finite-element methods of MATLAB's PDETOOLBOX and OOPDE toolbox.

In general, path-continuation procedures determine stationary solutions of a dynamical system combining prediction steps where a known steady-state solution is advanced in parameter space via a tangent predictor and correction steps where Newton procedures are used to converge to the next solution at a new value of the primary continuation parameter [23,24]. In this way one can start at, e.g., a numerically given solution, continue it in parameter space, and obtain a solution branch including its stability. The primary continuation parameter is in our case the gain parameter g, whereas the corresponding spectral parameter ω is used as an additional free parameter that is automatically adapted to the corresponding g during continuation. Further, one needs an additional auxiliary condition to break the phase-shift symmetry of the system in question in order to prevent the continuation algorithm from trivially following solutions along the corresponding degree of freedom. This condition can be easily implemented by, e.g., setting the phase of the LS to zero in the center of the computational domain.

To increase computational efficiency in two dimensions, we exploit the rotational symmetry of the LS and compute only one quarter of the physical domain $\Omega_2 = [-L_u, L_u]\times[-L_v, L_v]$, with $L_u = L_v = 90$, using a grid with $N_u \times N_v$ mesh points, $N_u = N_v = 256$. As a result Neumann boundary conditions are imposed in both the u and v directions, whereas periodic boundary conditions are employed in the one-dimensional case. There, the continuation is performed on the one-dimensional domain $\Omega_1 = [-L_u, L_u]$ with $L_u = 90$ using $N_u = 512$ equidistant mesh points.

b. Evolution of the folding point of the LS with q and s

In this section we discuss the influence of the system parameters, e.g., the normalized absorption q and the saturation parameter s, on the behavior of the SN point $g = g_{SN}$ of the single-LS branch in both one and two spatial dimensions. To this aim we perform one- and two-dimensional fold continuations for different q and s, and our results are presented in Fig. 10.

Figure 10(a) shows the continuation of the folding point g_{SN} as a function of q, obtained for different values of s, while in Fig. 10(b) fold continuation of g_{SN} as a function of s, for different values of q, is presented. Dashed (solid) lines in both panels indicate one- (two-) dimensional continuation. Note that the two-dimensional folding point is always shifted to higher current values compared with the one-dimensional case, but the overall evolution of the folding point g_{SN} remains the same. Furthermore, the behavior of g_{SN} with q and s follows the same trends as the homogeneous solution (see Sec. A 2), including its asymptotic behavior in the limit of large saturation and large absorption. That is, our predictions for the folding point evolution of the homogeneous solution hold for the folding point of the LS solution.

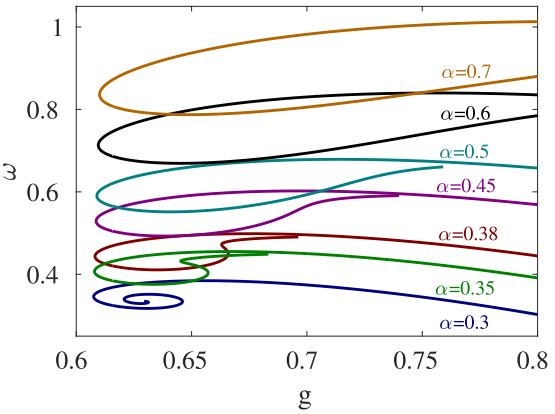

FIG. 11. One-dimensional bifurcation diagram of Eq. (9) in the (g,ω) plane calculated for increasing values of α at fixed $\beta = 0.5$. For small α the branch of a single LS forms a spiral which unfolds for increasing α. Different colors correspond to different values of α. Other parameters are the same as in Fig. 2.

c. Unfolding of the spiral

Figure 11 shows the typical spiral shape obtained for the branch of a LS in the (g,ω) plane at low values of α. One can see that the spiral shape of the LS branch remains well preserved for small values of α (see Fig. 11 for $\alpha = 0.3$). However, for increasing α the morphology of the branch changes: Beyond a certain threshold, the end point of the spiral curve moves to higher gain values (see Fig. 11 for $\alpha = 0.35,\ldots,0.5$), leading to the unfolding of the spiral ($\alpha = 0.6,0.7$). There, the resulting branch bifurcates from the threshold $g = 1$, exhibits a fold at a certain g, and continues towards higher gain values; that is, it coexists with the upper subbranch and always exhibits smaller ω. This branch morphology remains for ascending α, as shown in Fig. 2.

4. Numerical simulation of the Haus equation

We solved Eqs. (1)–(3) by adding two additional free parameters, ω and υ, which correspond to the oscillation frequency and the drift velocity of the solution along the propagation axis. In other words, the round-trip of the LBs presents a small deviation with respect to the cold-cavity round-trip time that corresponds to a drift υ in the reference frame of the cold cavity where one takes a snapshot every round-trip time (see [15] for more details). As such, Eq. (1) is rewritten as

$$\partial_\sigma E = (O_1 + O_2)E, \tag{A14}$$

with the two operators $O_{1,2}$ defined as

$$O_1 = \sqrt{\kappa}\left[\frac{1-i\alpha}{2}G(r_\perp,z,\sigma) - \frac{1-i\beta}{2}Q(r_\perp,z,\sigma)\right] + \sqrt{\kappa} - 1 + i\omega, \tag{A15}$$

$$O_2 = \frac{1}{2\gamma^2}\partial_z^2 + (d+i)\Delta_\perp + \upsilon\partial_z. \tag{A16}$$

The values of the free parameters (ω,υ) are adapted during the time integration via a simple control loop, allowing us to determine the frequency by looking at the phase variation of the peak of the LB and the drift along the propagation axis of the intensity profile averaged over the transverse dimension(s). In particular, canceling the natural drift of the solution along the propagation axis by a proper value of υ allows us to maintain the position of the LB close to the center of the numerical domain.

We solved Eq. (A14) using a semi-implicit split-step method in which the spatial operator O_2 is evaluated in Fourier space. Denoting $\tilde{O}_2$ the differential operator in Fourier space, the update sequence reads

$$E_1 = E_n(1 + \Delta t \times O_1), \tag{A17}$$

$$E_2 = \mathcal{F}^{-1}[e^{\Delta t \times \tilde{O}_2}\mathcal{F}[E_1]], \tag{A18}$$

$$E_{n+1} = E_2/(1 - \Delta t \times O_1). \tag{A19}$$

As the carrier variables G and Q are not dependent on the slow time, since we exploited the long-cavity limit, the operator O_1 can be obtained from the integration of Eqs. (2) and (3) by knowing the preexisting field intensity distribution and using Dirichlet boundary conditions at the beginning of the integration domain that reads

$$(G,Q)(r_\perp, z=0) = (G_0, Q_0). \tag{A20}$$

We used a physical domain $\Omega_H = [-L_x,L_x]\times[-L_y,L_y]\times[-L_z,L_z]$, with $L_{x,y} = 160$ and $L_z = 3$, using a grid with $N_x \times N_y \times N_z$ mesh points and $N_{x,y,z} = 128$. Periodic boundary conditions are automatically imposed in both the x,y directions as a consequence of the differentiation in Fourier space. We applied standard dealiasing with a 2/3 rule to the Fourier operator. As the Fourier operator $\mathcal{O}_2$ is linear, no dealiasing is needed. As such, one has to put dealiasing into $\mathcal{O}_1$ every time one goes into the Fourier space, and we apply the 2/3 rule in $\mathcal{F}[E_1]$ only in Eq. (A18).

The time step was $\delta t = 0.1$, which gives indistinguishable results for the LB parameters like energy, width, frequency, and velocity compared to those for smaller time steps. The main reason for this strong convergence property stems from the fact that around a steady state $O_1 \simeq 0$, while the spatial operator O_2 is obtained via exponential differencing and is therefore exact. As such, the remaining errors stems only from the operator splitting. It is proportional to a commutator that reads $[1 \pm \Delta t \times O_1, e^{\Delta t \times \tilde{O}_2}] \simeq 0$ since $O_1 \simeq 0$ at steady state. A convergence analysis of the numerical method yielded the expected second-order accuracy. Finally, we added to the field equation white Gaussian noise with variance $\xi = 10^{-4}$ mainly to accelerate the escape from unstable solutions and to avoid the detection of a false positive. The time integration was $\Delta\sigma = 3\times10^3$.

The numerical bifurcation diagrams were obtained by increasing g from a minimal value $g = 0.4$ up to $g = 1$ with a step of $\delta g = 2\times10^{-3}$. As initial conditions, we used a spherical solution $E_i(x,y,z) = E_0$, with (x,y,z) verifying the relation

$$\left(\frac{x}{L_x}\right)^2 + \left(\frac{y}{L_y}\right)^2 + \left(\frac{z}{L_x}\right)^2 < 1, \tag{A21}$$

with parameters $L_x = L_y = 10$, $L_z = 0.26$, and $E_0 = 1$. After an integration time of $\Delta\sigma$, if a stable LB solution is found, it is used as an initial condition for the next value of g. After the

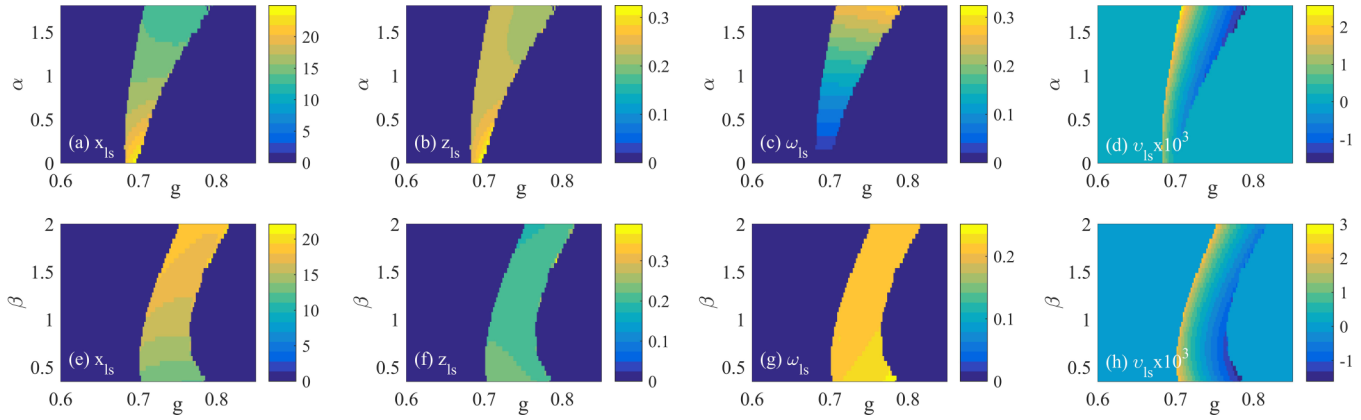

FIG. 12. Two-dimensional bifurcation diagrams showing the region of stable existence of the LBs by integrating the two-dimensional Haus equations (1)–(3) as a function of the gain g and the parameters α (top) and β (bottom). We represent (a) and (e) the FWHM in x, (b) and (f) the FWHM in z, (c) and (g) the frequency of the solution, and (d) and (h) the drift velocity. As mentioned in the main text, the range of stability increases with α and decreases for small values of β, in agreement with Fig. 4. Other parameters are $(s,\gamma,\kappa,\Gamma,Q_0,d) = (30,40,0.8,0.04,0.3,10^{-2})$ and (a)–(d) $\beta = 0.5$ and (e)–(h) $\alpha = 1.5$.

entire upward scan in g, the solution branch is further extended via continuation downward from the first point that was found using the spherical IC. This method allows us to get a good approximation of the folding point limiting the branch at low values of g. However, during such "blind" parameter sweeps, a large fraction of the simulations consists of a dynamics in which the field goes down to $E = 0$ or the spatiotemporal profile explodes and invades the full numerical domain. As such, special flags were introduced to cut the time integration. This simple procedure diminishes the computation times by several orders of magnitude. The scans along q were performed with a step $\delta q = 3\times10^{-2}$. Simulations were performed using 100 cores of Xeon E5 CPUs on a HPC cluster Bull B510.

The results of the scan in the (α,g), (β,g) and (g,q) planes are depicted in Figs. 12 and 13, where we represent the characteristics of the LBs, such as their FWHM in the transverse and longitudinal directions, the residual frequency, and the velocity of motion along the propagation axis. As mentioned in the main text, the stability region increases with larger values of α and smaller values of β, while too large values of s are detrimental.

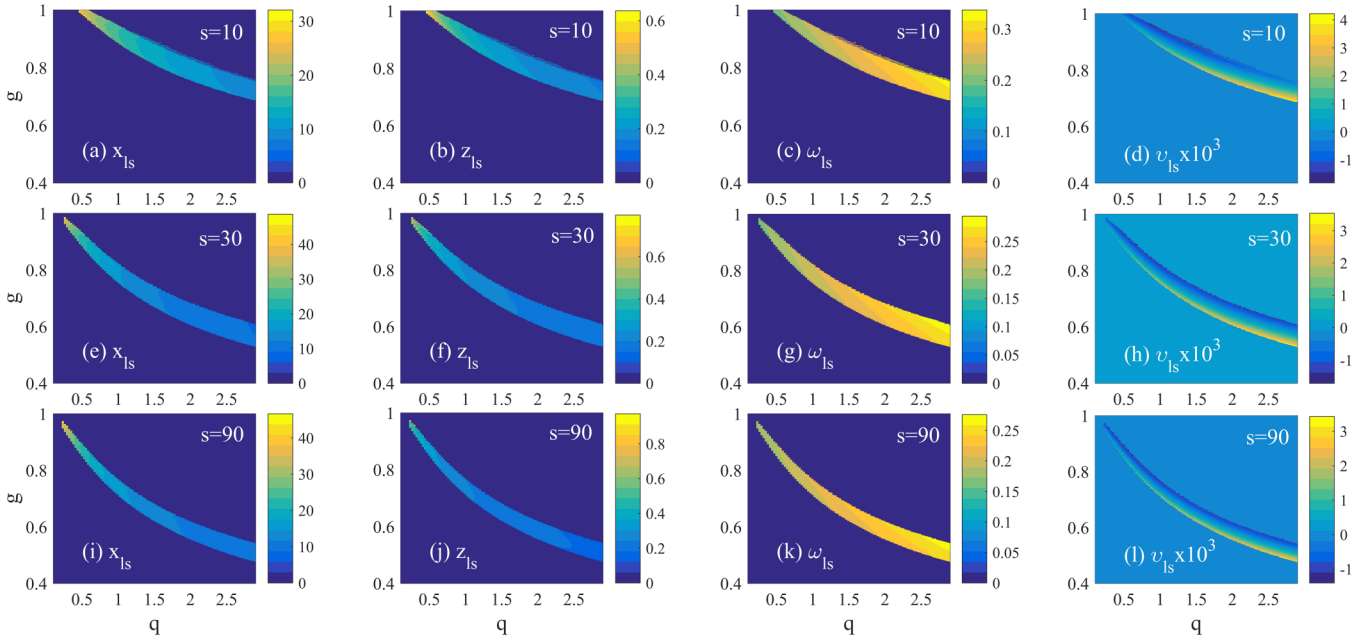

FIG. 13. Two-dimensional bifurcation diagram showing the region of stable existence of the LBs by integrating the two-dimensional Haus equation Eqs. (1)–(3) as a function of the gain g and the absorption q parameters, for increasing values of s. The top, central and bottom lines correspond to $s = 10$, $s = 30$, and $s = 90$, respectively. We represent (a,e,i) the FWHM in x, (b,f,j) the FWHM in z, (c,g,k) the frequency of the solution, and (d,h,l) the drift velocity. As mentioned in the main text, the range of stability decreases with larger values of s. Other parameters are $(\alpha,\beta,\gamma,\kappa,\Gamma,d) = (1.5,0.5,40,0.8,0.04,10^{-2})$.

[1] Y. Silberberg, Collapse of optical pulses, Opt. Lett. **15**, 1282 (1990).

[2] V. E. Zakharov, Collapse of Langmuir Waves, Sov. Phys. JETP **35**, 908 (1972).

[3] M. Tlidi and P. Mandel, Space-time localized structures in the degenerate optical parametric oscillator, Phys. Rev. A **59**, R2575 (1999).

[4] N. Veretenov, A. Vladimirov, N. Kaliteevskii, N. Rozanov, S. Fedorov, and A. Shatsev, Conditions for the existence of laser bullets, Opt. Spectrosc. **89**, 380 (2000).

[5] M. Brambilla, T. Maggipinto, G. Patera, and L. Columbo, Cavity Light Bullets: Three-Dimensional Localized Structures in a Nonlinear Optical Resonator, Phys. Rev. Lett. **93**, 203901 (2004).

[6] L. Columbo, I. M. Perrini, T. Maggipinto, and M. Brambilla, 3D self-organized patterns in the field profile of a semiconductor resonator, New J. Phys. **8**, 312 (2006).

[7] M. Marconi, J. Javaloyes, S. Balle, and M. Giudici, How Lasing Localized Structures Evolve Out of Passive Mode Locking, Phys. Rev. Lett. **112**, 223901 (2014).

[8] H. A. Haus, Mode-locking of lasers, IEEE J. Sel. Top. Quantum Electron. **6**, 1173 (2000).

[9] J. Javaloyes, Cavity Light Bullets in Passively Mode-Locked Semiconductor Lasers, Phys. Rev. Lett. **116**, 043901 (2016).

[10] N. N. Rosanov and S. V. Fedorov, Diffraction switching waves and autosolitons in a saturable-absorber laser, Opt. Spectrosc. **72**, 782 (1992).

[11] H. Uecker, D. Wetzel, and J. D. M. Rademacher, pde2path – A Matlab package for continuation and bifurcation in 2D elliptic systems, Numer. Math. Theory Methods Appl. **7**, 58 (2014).

[12] P. Genevet, S. Barland, M. Giudici, and J. R. Tredicce, Cavity Soliton Laser Based on Mutually Coupled Semiconductor Microresonators, Phys. Rev. Lett. **101**, 123905 (2008).

[13] M. Brambilla, L. A. Lugiato, F. Prati, L. Spinelli, and W. J. Firth, Spatial Soliton Pixels in Semiconductor Devices, Phys. Rev. Lett. **79**, 2042 (1997).

[14] M. Marconi, J. Javaloyes, S. Balle, and M. Giudici, Passive mode-locking and tilted waves in broad-area vertical-cavity surface-emitting lasers, IEEE J. Sel. Top. Quantum Electron. **21**, 85 (2015).

[15] J. Javaloyes, P. Camelin, M. Marconi, and M. Giudici, Dynamics of Localized Structures in Systems with Broken Parity Symmetry, Phys. Rev. Lett. **116**, 133901 (2016).

[16] G. New, Pulse evolution in mode-locked quasi-continuous lasers, IEEE J. Quantum Electron. **10**, 115 (1974).

[17] A. G. Vladimirov, S. V. Fedorov, N. A. Kaliteevskii, G. V. Khodova, and N. N. Rosanov, Numerical investigation of laser localized structures, J. Opt. B **1**, 101 (1999).

[18] T. Dohnal, J. Rademacher, H. Uecker, and D. Wetzel, pde2path-version 2.0: faster fem, multi-parameter continuation, nonlinear boundary conditions, and periodic domains-a short manual, arXiv:1409.3119.

[19] A. G. Vladimirov, N. N. Rozanov, S. V. Fedorov, and G. V. Khodova, Bifurcation analysis of laser autosolitons, Quantum Electron. **27**, 949 (1997).

[20] A. G. Vladimirov, N. N. Rozanov, S. V. Fedorov, and G. V. Khodova, Analysis of the stability of laser solitons, Quantum Electron. **28**, 55 (1998).

[21] See Supplemental Material at http://link.aps.org/supplemental/10.1103/PhysRevA.96.023821 for the videos depicting the various modes of instability governing the dynamics of the Rosanov equations in one and two dimensions as well as those of the Haus equations in two and three dimensions.

[22] A. G. Vladimirov and D. Turaev, Model for passive mode locking in semiconductor lasers, Phys. Rev. A **72**, 033808 (2005).

[23] R. Seydel, *Practical Bifurcation and Stability Analysis*, 3rd ed., Interdisciplinary Applied Mathematics (Springer, New York, 2010).

[24] Y. A. Kuznetsov, *Elements of Applied Bifurcation Theory*, 2nd ed., Applied Mathematical Sciences (Springer, New York, 1998).